

Measurements of three exo-planetesimal compositions: a planetary core, a chondritic body, and an icy Kuiper belt analogue

Jamie T. Williams^{1, *}, Boris T. Gänsicke¹, Snehalata Sahu¹, David J. Wilson², Detlev Koester³, Andrew M. Buchan¹, Odette Toloza⁴, Yuqi Li⁵, and Jay Farihi⁶

¹ Department of Physics, University of Warwick, Coventry, CV4 7AL, UK

² Laboratory for Atmospheric and Space Physics, University of Colorado, Boulder, CO 80303

³ Institut für Theoretische Physik und Astrophysik, University of Kiel, 24098 Kiel, Germany

⁴ Departamento de Física, Universidad Técnica Federico Santa María, Avenida España 1680, Valparaíso, Chile

⁵ Institute of Astronomy, University of Cambridge, Madingley Road, Cambridge, CB3 0HA, UK

⁶ Department of Physics and Astronomy, University College London, London WC1E 6BT, UK

Accepted XXX. Received YYY; in original form ZZZ

ABSTRACT

The study of planetesimal debris accreted by white dwarfs offers unique insights into the composition of exoplanets. Using far-ultraviolet and optical spectroscopy, we have analysed the composition of planetesimals accreted by three metal enriched H-dominated white dwarfs with effective temperatures of $T_{\text{eff}} \approx 20\,000$ K. WD 0059+257 is accreting an object composed of 71.8 ± 7.9 per cent Fe and Ni by mass, indicating a large core mass fraction of 69 per cent, similar to that of Mercury. We model this planetesimal as having a differentiated Earth-like composition with 65 per cent of its mantle stripped, and we find this mass loss can be caused by vaporisation of the planetesimal’s mantle during post-main sequence evolution. The tentative S detection in WD 0059+257 is a possible clue to the nature of the light element in planetary cores, including that of the Earth. The volatile-rich composition of WD 1943+163 is consistent with accretion of a carbonaceous chondrite-like object, but with an extreme Si depletion. WD 1953–715 accretes a planetesimal which contains 64 ± 21 per cent of O in the form of ices, likely H₂O. This body therefore requires an initial orbit at formation beyond a radial distance of $\gtrsim 100$ au for ice survival into the white dwarf phase. These three planetary enriched white dwarfs provide evidence of differing core fractions, volatile budgets, and initial orbital separations of the accreted planetesimals, all of which help us understand their formation and evolutionary history.

Key words: white dwarfs – planets and satellites: interiors – planets and satellites: composition

1 INTRODUCTION

White dwarfs are the bare cores of stars, formed following the end of nuclear fusion and subsequent ejection of their outer layers. A key characteristic of white dwarfs is their strong surface gravity, $\log g \approx 8$, resulting from their mass of $\approx 0.6 M_{\odot}$ contained within an object approximately the size of the Earth. This leads to elements heavier than He rapidly sinking, resulting in a pristine H or He envelope (e.g. Schatzman 1949). Traces of metals in white dwarf atmospheres have been linked to the accretion of planetary material, with 44 ± 6 per cent of warm (with effective temperatures of $13\,000 < T_{\text{eff}} < 30\,000$ K) H-dominated atmosphere white dwarfs showing evidence of active accretion (Koester et al. 2014; Ould Rouis et al. 2024).

By analysing spectroscopic observations of white dwarfs enriched by planetary material, the composition of the accreted material can be inferred (e.g. Zuckerman et al. 2007; Gänsicke et al. 2012; Swan et al. 2019; Rogers et al. 2024). Unlike the studies of planets around main sequence stars where the only insight into planetary interior compositions is their bulk density (e.g. Valencia et al. 2006) and considering that interior models can be highly degenerate (e.g. Dorn

et al. 2015), white dwarfs can reveal the make-up of planets. Investigations into individual planetary enriched white dwarfs have revealed a large diversity, including bulk Earth-like objects (e.g. Klein et al. 2010; Xu et al. 2014; Doyle et al. 2023; Swan et al. 2023), core-rich fragments (e.g. Melis et al. 2011; Wilson et al. 2015), mantle and crust-rich fragments (e.g. Zuckerman et al. 2011; Hollands et al. 2021), and volatile-rich Kuiper Belt-like objects (e.g. Xu et al. 2017; Johnson et al. 2022). This method has been used to find evidence of rocky planetesimal formation at a variety of radial locations (Harrison et al. 2018) and to infer the occurrence rate of differentiation¹ among accreted planetesimals (Bonsor et al. 2020).

Photospheric abundances can only directly reflect the composition of the parent body if the accretion rate varies on timescales longer than the one which metals diffuse out of the atmosphere. With diffusion times on the scale of days, this is always true for warm ($T_{\text{eff}} \gtrsim 15\,000$ K), H-dominated atmosphere white dwarfs (Koester 2009). Additionally, warm white dwarfs are our only opportunity to simultaneously detect the key rock-forming metals O, Mg, Si, and Fe (Williams et al. 2024) which comprise 95 per cent of the mass

¹ Defined as the segregation of chemically distinct rock phases into layers, in the case of exoplanets into a core, mantle, and crust.

* E-mail: jamietwilliams.astro@gmail.com

of bulk Earth (Lodders 2003). Here, we present the analysis of three such stars (WD 0059+257, WD 1943+163, and WD 1953–715) using high-resolution optical and medium-resolution far-ultraviolet (FUV) spectroscopy. These three white dwarfs were identified as being actively accreting planetary debris because of their large photospheric C and Si abundances (Koester et al. 2014). Additional measurements of their O abundance implied that their C/O ratios were consistent with Solar System objects (Wilson et al. 2016). In this paper, we present the full complement of detected metals and use these to interpret the nature of the accreted planetesimals.

2 OBSERVATIONS

WD 0059+257, WD 1943+163 and WD 1953–715 were observed in the FUV with the Cosmic Origins Spectrograph onboard the *Hubble Space Telescope* (HST/COS, Green et al. 2012) using the G130M grating (Table 1). The central wavelength used was 1291 Å which covers the wavelength range 1132–1433 Å with a gap between 1278 and 1288 Å due to a space between the detector segments. We masked the Lyman- α airglow emission present in the region 1213.5–1217 Å.

Optical spectroscopy of the three stars was performed using the Ultraviolet and Visual Echelle Spectrograph mounted on the Very Large Telescope (VLT/UVES, Dekker et al. 2000). These observations were reduced using the REFLEX reduction tool developed by ESO (Freudling et al. 2013). Telluric corrections were applied using the MOLECFIT package (Smette et al. 2015; Kausch et al. 2015) and the individual exposures were co-added to a single spectrum. The blue arm UVES spectra (3760–4990 Å) contains all metal lines detected in the optical. We inspected the red arm UVES spectra (5700–9300 Å) for O I 7774 Å absorption and Ca II infrared triplet emission from the gaseous component of a debris disc (e.g. Gänsicke et al. 2006), but did not detect either feature in any of our targets. No infrared excesses were detected in these three white dwarfs by *Spitzer* (Rocchetto et al. 2015), although the debris may have optically thin dust or an unfavourable inclination which limits its detectable emission (Bonsor et al. 2017).

3 METHODS

3.1 Photospheric abundances

We detect a wide range of photospheric metals in WD 0059+257 (O, Mg, Si, S, Ca, Fe, and Ni) as well as in WD 1943+163 and WD 1953–715 (C, O, Mg, Si, S, Ca, and Fe). To fit the abundances of these elements, and to determine upper limits for N, Al, P, and Cr, we used atmosphere models and synthetic spectra computed with the code described by Koester (2010) but with numerous updates and improvements to the equation of state and absorption coefficients. The most important developments are the inclusion of non-ideal effects in the diffusion equation, new calculations for the collision integrals, and significant changes to the diffusion and envelope code (Koester et al. 2020). The absorption lines used in the analysis are summarised in Table A1. Fixing the T_{eff} and $\log g$ to the values determined by Sahu et al. (2023, see Table 2), we created a grid of models for each of the elements listed above with abundances in the range $-10 < \log(Z/H) < -4$ in steps of 0.25 dex. The model fluxes were interpolated and scaled to the white dwarf radius and distance (based on inverting the *Gaia* DR3 parallax) to find a best match to the observed spectra. When we fit to individual lines, we allowed a small flux offset, normalising around the lines under analysis using

a χ^2 minimisation technique. The interstellar lines were also modelled (Section 3.1.1) to obtain accurate metal abundances. Initially, the best-fit abundances were determined for each element using a model grid that contained only lines of that element. Because a number of wavelength regions contain blended lines, we then computed new model grids using the preliminary best-fit metal abundances for all elements and re-fitted the spectra varying the abundance of one element at a time. We continued this iterative process until the abundances converged. The final model fits to the COS spectra are illustrated in Fig. 1 and to the UVES spectra in Fig. 2, with the resulting photospheric number abundances listed in Table 3.

3.1.1 ISM line fitting

Some of the photospheric metal lines in the FUV are contaminated by absorption in the interstellar medium (ISM) which can affect the abundance measurements. Given the COS velocity resolution of $\approx 15 \text{ km s}^{-1}$, these ISM lines may either be resolved or blended with the photospheric lines, depending on the line of sight velocity of the ISM and the systemic velocity and the gravitational redshift of the white dwarf. Hence, to determine accurate abundances, the contribution of the ISM lines must be included in the fits to the photospheric lines. We modelled the ISM lines using Gaussian functions where the free parameters are their amplitudes, standard deviation, and centroids of the velocity, where we restricted the widths to be within the range of 0.01 – 0.03 Å corresponding to a velocity dispersion of 3 – 7 km s^{-1} . This is a reasonable approximation considering the warm temperature of the local ISM ($\approx 7000 \text{ K}$, Redfield & Linsky 2004) and the presence of one to two ISM clouds along the line of sight (Malamut et al. 2014). We list the ISM line velocities for each modelled species in Table 4. To confirm that our fitting of blended ISM and photospheric lines gives reliable abundances, we compare their results with those of uncontaminated lines of the same element. In all cases, we find that their radial velocities and abundances agree.

3.1.2 Abundance errors

The errors on abundances were computed using different methods, depending on the number of lines available. For Si, Fe, and Ni, multiple lines were detected in the data, so we fitted each line individually and adopted the weighted mean of individual measurements as the abundance and the standard deviation of the measurements as the error. This method accounts for the statistical error in the fit, systematic uncertainties in the data (via the flux normalisation) and errors in the atomic line data used in the atmosphere models.

Ca and Mg both only have a single line detected in the data, and in the case of C, O, and S the overlap between transitions of different elements required them to be fitted simultaneously. We first obtained the statistical errors in the fits from the covariance matrices but found them to be unrealistically small. To estimate the magnitude of the true error, we use the Planetary Enriched White Dwarf Database² (PEWDD, Williams et al. 2024). We selected H-dominated atmosphere white dwarfs with $15000 < T_{\text{eff}} < 25000 \text{ K}$ and multiple published abundance analyses. The spread in the published abundances are representative of the overall systematic uncertainties in the abundances due to differences in the atmospheric parameters T_{eff} and $\log g$, instruments and models on which these analyses were based, and the fitting procedures that were used. The number of white dwarfs which fulfil these criteria are four for C, O, and S, 13 for Mg,

² <https://github.com/jamietwilliams/PEWDD>

Table 1. Observations log for spectra used in this paper.

Name	Date	Instrument	Start Time	Exposure Time (s)	Wavelength Range (Å)	S/N	Resolving power ($\lambda/\Delta\lambda$)
WD 0059+257	2011-01-22	<i>HST</i> /COS	14:39:13	1140	1132–1274, 1291–1433	23	12 000–16 000
	2013-07-13	VLT/UVES	09:00:45	2980	3700–5000	41	$\approx 40\,000$
	2013-08-19		06:18:45	2980			
WD 1943+163	2011-04-03	<i>HST</i> /COS	00:42:19	600	1132–1274, 1291–1433	35	12 000–16 000
	2013-06-20	VLT/UVES	06:20:08	2980	3700–5000	87	$\approx 40\,000$
	2013-06-21		07:36:26	2980			
WD 1953–715	2011-05-17	<i>HST</i> /COS	19:19:42	1100	1132–1274, 1291–1433	28	12 000–16 000
	2013-08-02	VLT/UVES	06:06:10	2980	3700–5000	59	$\approx 40\,000$
	2013-08-13		00:41:51	2980			

and 16 for Ca, and we use the median of the spread in the abundances of a given element as an estimate of the systematic error, which is added in quadrature to the statistical error.

3.1.3 Upper limits

We do not detect N, Al, P, or Cr in the atmospheres of any of the three white dwarfs. We also do not detect C in WD 0059+257 and Ni in WD 1943+163 and WD 1953–715, however, we have determined upper limits on their abundances following the procedure of [Hollands et al. \(2020\)](#). We selected the spectral region where a photospheric line is expected and compared it with a grid of synthetic spectra, including the ISM model wherever required. We varied the model abundances by 0.01 dex and determined the χ^2 considering the uncertainties in the observed fluxes. The χ^2 values were then converted to likelihood considering Jeffrey’s prior and the cumulative distribution function (CDF) was computed. Finally, the abundance at the 99 per cent confidence interval of the CDF representing the 3σ detection threshold was chosen as the upper limit. This method is illustrated in Fig. 4 for determining the Al upper limit in WD 0059+257.

3.1.4 Notes on individual elements

The three O I lines at 1302.2 Å, 1304.9 Å, and 1306.0 Å are all affected by O airglow from the Earth’s atmosphere to varying degrees, with the former two also affected by ISM lines. Extracting only the data obtained during *HST*’s night-time can remove airglow, but WD 0059+257 and WD 1943+163 were only observed during the day-time. Therefore, to reduce the effect of airglow, we used the community-generated templates for O I lines³ ([Bourrier et al. 2018](#)). The templates were obtained with COS G130M grating and a central wavelengths of 1291 Å, hence with the same setup as our observations. The velocity and amplitude of the template airglow lines were varied to find a best match to those in our COS data, masking the strong absorption lines from Si II and O I in this process. The original and airglow corrected spectra for WD 1943+163 are shown in Fig. 3. After the airglow correction, we follow the procedure to fit the ISM and photospheric lines together. To confirm that the airglow minimisation and ISM lines did not alter the actual O abundance, we compared the results from regions affected by airglow and ISM to that of the unaffected O I 1152.2 Å line and found that the abundances differ by only 0.18, 0.12, and 0.3 dex for WD 0059+257, WD 1943+163, and WD 1953–715, respectively, with the photospheric line velocities being in excellent agreement, within 1σ .

The COS spectra contain many absorption lines of Si II and Si III

(Table A1). We measured the Si abundance selecting the spectral region 1293–1310 Å dominated by Si III absorption lines and found it to differ by 0.4–0.5 dex from the regions dominated by Si II lines. One of the reasons for the discrepancy could be due to the difficulty in accurately fitting the continuum region (local normalisation) affected by the presence of multiple strong Si III lines. The final Si abundance is the weighted average of the abundances determined from the Si II and Si III lines. In Fig. 1, we plot these average abundances, which explains the somewhat lower visual quality of the fits to Si III lines. The abundance error we quote adequately accounts for the discrepancy between the Si II and Si III lines.

We detect strong photospheric S II lines in WD 1943+163 and WD 1953–715 that are well resolved from the ISM lines. In the case of WD 0059+257, we notice a weak photospheric line from S II at ≈ 1259.5 Å. Fitting this line, we found that its velocity is consistent (within 1σ) with those derived from strong photospheric Si II lines, thus confirming the S detection in the atmosphere of WD 0059+257.

The *HST*/COS detector is affected by fixed pattern noise, which can be mitigated by using all four FP-POS settings. Because the observations analysed here were obtained as part of a snapshot program with strictly limited exposure times, we only used two FP-POS settings. The blue end of the COS spectrum is most strongly affected by the low signal-to-noise ratio (S/N), which explains the apparent visually poor fit of some of the Fe lines in that region.

3.1.5 Radial velocity

The radial velocities of the metal lines in the spectra of *HST*/COS and VLT/UVES do not agree within statistical uncertainties, which is particularly apparent for WD 1953–715 (see Table 3). The dominant source in the systematic uncertainties is the COS wavelength zero-point accuracy⁴, 15 km s^{-1} , which is sufficient to explain the discrepancy between the velocities measured with the two instruments. In addition, there are slight disagreements between the velocities of different elements detected with the same instrument, for example Fe exhibits lower velocities than the other elements in all three stars. Poor atomic data could result in inaccurate vacuum wavelengths and hence discrepant radial velocities. However, we do not have a satisfactory explanation for this mismatch.

3.2 Accretion rates

Because metals sink out of the atmosphere within days and accretion events last $\approx 10^4 - 10^6$ yrs ([Girven et al. 2012](#); [Cunningham et al. 2021](#)), it is a safe assumption that accretion is ongoing and in the steady-state phase. At the T_{eff} and $\log g$ of these white dwarfs,

³ <https://www.stsci.edu/HST/instrumentation/cos/calibration/airglow>

⁴ <https://hst-docs.stsci.edu/cosihb/chapter-5-spectroscopy-with-cos>

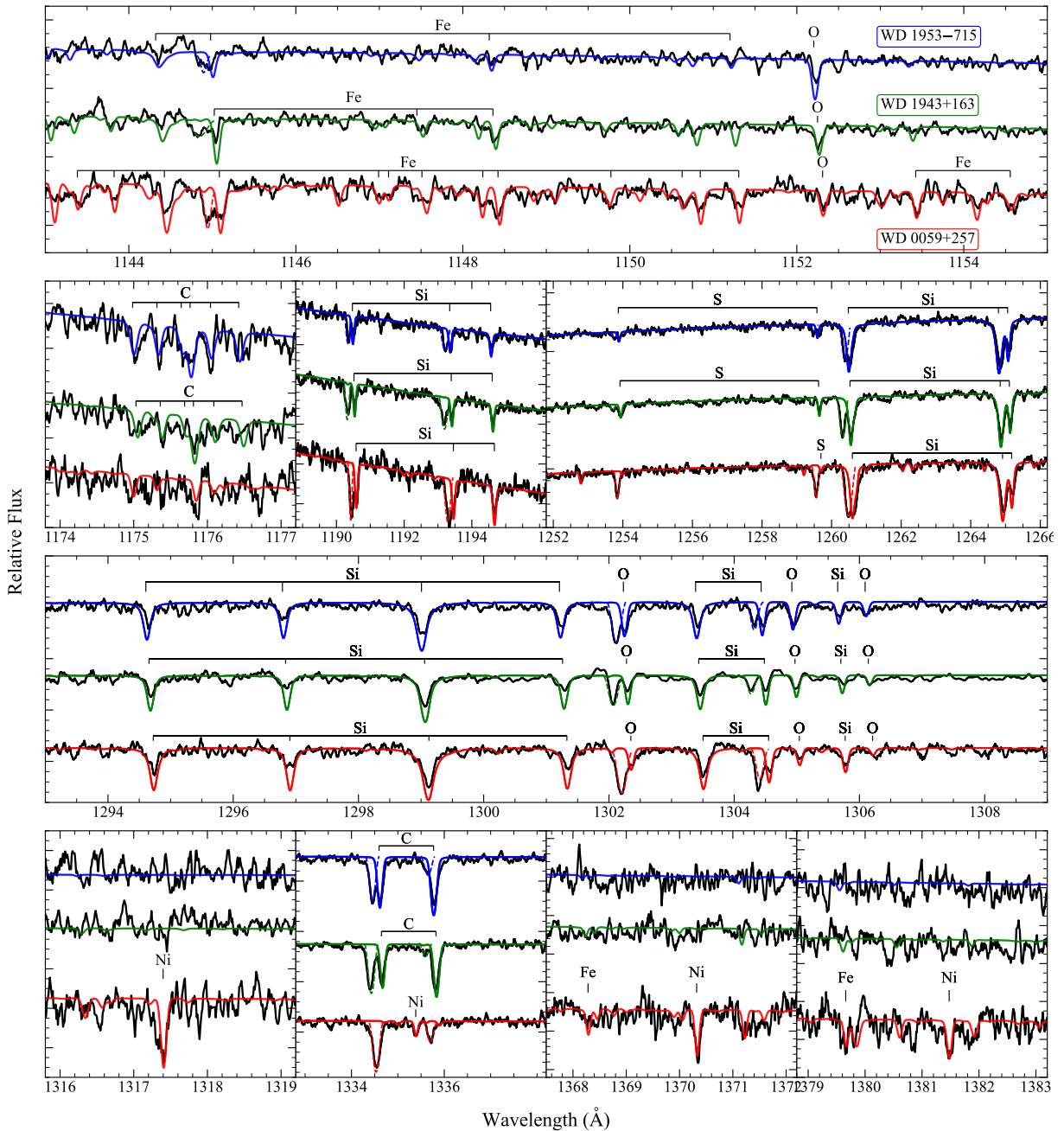


Figure 1. From top to bottom: *HST/COS* spectra (in black, smoothed with a five-point boxcar) of WD 1953–715, WD 1943+163 and WD 0059+257 and the best-fit models in blue, green and red, respectively. The spectra are offset in flux for clarity. The dashes represent which metal lines were used to measure the photospheric abundances. Absorption features in the models that are not marked were not used to fit abundances because they were too weak in the data. The dashed wavelength regions of the models include fits to the ISM lines. The spectra are shown in the observed wavelength frame, hence the photospheric absorption features do not line up with at their laboratory wavelengths. Because the metal abundances are an average of fitting to multiple lines, some lines appear to have a poor fit, particularly the Si III lines in the 1294 – 1306 Å region. This discrepancy is discussed in Section 3.1.4.

radiative levitation cannot sustain the observed metal abundances (see Figs. 5 and 6 in Koester et al. 2014) and hence we do not take this effect into account. The diffusion flux for each metal is constant throughout the atmosphere, and we take the observed abundance X_{acc} to be the approximate value at the Rosseland mean opacity $\tau_{\text{Ross}} = 2/3$ from which we calculate the accretion rate \dot{M}_{acc} using the equation (Koester et al. 2014):

$$X\rho v_{\text{diff}} = X_{\text{acc}}\dot{M}_{\text{acc}} \quad (1)$$

where X is the metal mass fraction determined from photospheric abundances, ρ the mass density in the atmosphere, and v_{diff} the diffusion velocity, both of which are computed from atmospheric models (Koester 2010). Accretion rates are listed in Table 3. All analysis in this paper is under the assumption of steady-state accretion.

Table 2. Stellar properties of the three white dwarfs analysed. Effective temperature (T_{eff}), surface gravity ($\log g$), white dwarf mass (M_{WD}), and cooling age (t_{cool}) are taken from [Sahu et al. \(2023\)](#). The quoted cooling age is the average of values using the Montreal ([Bédard et al. 2020](#)) and LPCODE ([Althaus et al. 2013; Camisassa et al. 2016, 2019](#)) sequences, with errors determined using the tables from [Pathak et al. \(2024\)](#). *Gaia* DR3 ID, parallaxes are taken from *Gaia* DR3 and distances inferred as inverse parallaxes.

Name	WD 0059+257	WD 1943+163	WD 1953–715
WD J Name	WD J010145.76+260242.70	WD J194531.76+162738.77	WD J195838.65-712343.50
<i>Gaia</i> DR3 ID	307372225052233984	1820678800528443776	6422236358302245248
T_{eff} (K)	$20\,110 \pm 40$	$19\,250 \pm 30$	$19\,250 \pm 60$
$\log g$ [cm s^{-2}]	7.89 ± 0.02	7.87 ± 0.01	8.12 ± 0.02
Parallax (milliarcsec)	9.20 ± 0.05	21.4 ± 0.05	14.34 ± 0.03
Distance (pc)	108.7 ± 0.6	46.8 ± 0.1	69.5 ± 0.1
M_{WD} (M_{\odot})	0.56 ± 0.01	0.55 ± 0.02	0.69 ± 0.02
t_{cool} (Myr)	52 ± 5	62 ± 5	106 ± 4

Table 3. Photospheric number abundances, $\log(Z/H)$, steady-state accretion rates, $\log(\dot{M}_{\text{acc,Z}})$ [g/s], and photospheric line radial velocities, v_Z of the three white dwarfs studied. The errors on radial velocities are an underestimate, since *HST/COS* has a wavelength accuracy of 15 km s^{-1} . The abundances of Mg and Ca were obtained using the ground-based VLT/UVES instrument and hence offset.

Z	WD 0059+257			WD 1943+163			WD 1953–715		
	$\log(Z/H)$	$\log \dot{M}_{\text{acc,Z}}$	v_Z (km s^{-1})	$\log(Z/H)$	$\log \dot{M}_{\text{acc,Z}}$	v_Z (km s^{-1})	$\log(Z/H)$	$\log \dot{M}_{\text{acc,Z}}$	v_Z (km s^{-1})
C	≤ -8.79	≤ 3.56		-6.37 ± 0.16	6.05	26.1 ± 2.3	-5.75 ± 0.16	6.80	19.7 ± 0.1
N	≤ -5.98	≤ 6.62		≤ -6.28	≤ 6.44		≤ -5.32	≤ 7.47	
O	-5.72 ± 0.14	7.03	44.2 ± 0.6	-5.70 ± 0.13	7.28	30.2 ± 1.7	-5.51 ± 0.19	7.47	22.3 ± 0.9
Mg	-5.84 ± 0.14	6.71	46.3 ± 1.5	-5.64 ± 0.14	6.87	31.4 ± 1.5	-6.35 ± 0.14	6.31	9.9 ± 1.5
Al	≤ -6.97	≤ 5.67		≤ -7.15	≤ 5.57		≤ -6.78	≤ 6.04	
Si	-6.26 ± 0.24	6.43	47.0 ± 3.3	-6.57 ± 0.25	6.25	32.2 ± 0.9	-6.39 ± 0.22	6.49	25.3 ± 2.0
P	≤ -7.70	≤ 5.11		≤ -8.39	≤ 4.64		≤ -8.01	≤ 5.05	
S	-7.33 ± 0.29	5.60	49.8 ± 1.0	-6.54 ± 0.10	6.64	31.3 ± 0.5	-6.66 ± 0.12	6.59	27.2 ± 0.7
Ca	-6.71 ± 0.18	6.27	42.9 ± 1.0	-7.01 ± 0.18	5.88	35.0 ± 0.2	-7.63 ± 0.18	5.45	6.5 ± 1.0
Cr	≤ -6.59	≤ 6.61		≤ -6.85	≤ 6.35		≤ -6.54	≤ 6.78	
Fe	-5.54 ± 0.16	7.73	41.4 ± 0.6	-6.22 ± 0.17	7.09	25.4 ± 1.1	-6.43 ± 0.19	6.98	16.7 ± 2.1
Ni	-6.80 ± 0.24	6.53	42.3 ± 3.2	≤ -7.60	≤ 5.82		≤ -7.64	≤ 5.85	
Σ		7.89			7.67			7.74	

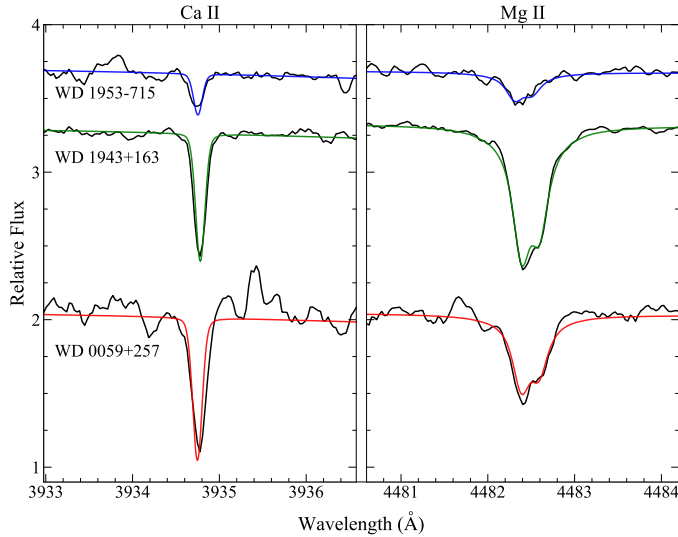


Figure 2. From top to bottom: normalised UVES spectra (in black, smoothed with a five-point boxcar and offset for clarity) of WD 1953–715, WD 1943+163 and WD 0059+257 along with the best-fit models in blue, green, and red, respectively showing the Ca II (left) and Mg II (right) lines. The spectra have been shifted to centre the lines at their vacuum wavelengths.

Table 4. ISM line velocities for relevant ions.

Ion	v_{ISM} (km s^{-1})		
	WD 0059+257	WD 1943+163	WD 1953–715
C II	1.8 ± 0.5	-28.3 ± 0.3	-17.2 ± 0.5
N I	7.9 ± 2.0	-25.0 ± 1.7	-12.1 ± 2.6
O I	5.8 ± 0.5	-23.1 ± 0.5	-12.4 ± 0.6
Si II	11.1 ± 4.1	-24.5 ± 0.8	-12.4 ± 1.5
S II	12.4 ± 0.6	-25.3 ± 0.5	-9.7 ± 0.8
Fe II	1.7 ± 1.7	-30.6 ± 2.6	-8.2 ± 3.9

4 MANTLE LOSS

Enhanced stellar luminosity during post-main sequence evolution can alter the composition of planetesimals. Previous studies indicate that this increased luminosity can induce heating and subsequent melting, which leads to differentiation, albeit only for radii $\leq 30 \text{ km}$ and originally orbiting within $\approx 2 \text{ au}$ ([Li et al. 2024](#)). Here, we investigate the feasibility of a similar process: direct melting during the post-main sequence phase causing the vaporisation and loss of mantle material, which would result in a core-rich planetesimal. [Vanderburg et al. \(2015\)](#) explored mass loss of a planetesimal orbiting close to a white dwarf, and found the rates were sufficient to explain the dust clouds and accretion onto WD 1145+017. We expand this treatment over the entire post main sequence evolution (in particular the red giant branch, horizontal branch and asymptotic giant branch phases).

We used MESA stellar evolution models for stars of masses $M_0 = 1 M_{\odot}$, $2 M_{\odot}$, and $2.5 M_{\odot}$ ([Dotter 2016; Choi et al. 2016; Paxton](#)

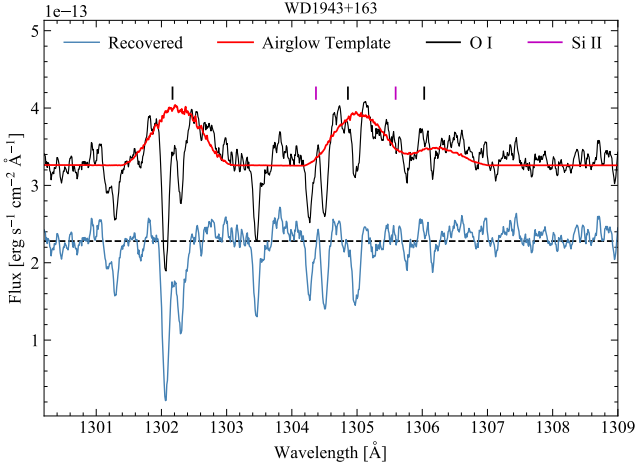


Figure 3. *HST* COS spectrum of WD 1943+163 in the region affected by airglow, before (black line) and after (blue line) we apply the airglow correction as described in Section 3.1.4. The best-fit airglow template for the raw spectrum is shown as a solid red line. For clarity, the corrected spectrum is slightly offset downwards in flux, with the dashed black line showing the continuum. Correction for airglow is required for an accurate determination of the abundances of O I (black dashes) and Si II (pink dashes) which have photospheric absorption lines within this wavelength region.

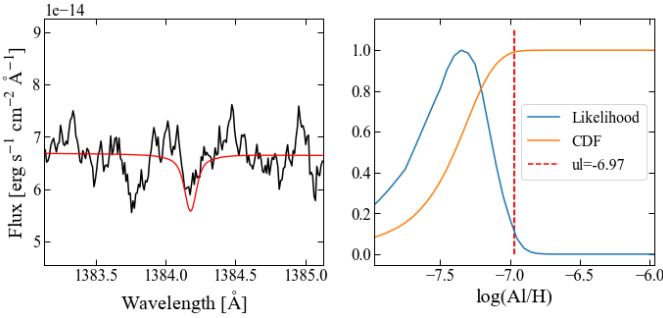


Figure 4. An example illustrating the determination of upper limits on the photospheric abundances. The left panel shows the data around the Al III line at 1384.1 Å in black, with a model fit at the Al upper limit overlaid in red. The right panel shows the CDF (orange) of the likelihood (blue) as a function of the Al abundance. We define the upper limit (ul) as being the 99th (3σ) percentile of the CDF, which is the maximum number abundance possible without returning a statistically significant detection.

et al. 2011, 2013, 2015, 2018) with a metallicity of $Z = 0.02$. During the post main sequence evolution, the star loses mass, causing the orbits of planetesimals⁵ to widen. We assume that the stellar mass loss is adiabatic and isotropic and that radiation and sublimation perturbations are negligible. We do not consider any additional sources of perturbations such as gravitational interactions with planets in this model. Assuming a circular orbit⁶, the semimajor axis, a_i , evolves as:

$$a_i = a_0 \left(\frac{M_0}{M_i} \right) \quad (2)$$

⁵ We refer to planetesimals as objects with masses $\lesssim M_{\text{Ceres}}$

⁶ An eccentric orbit leads to a maximum increase in effective temperature by ≈ 10 per cent for the same semimajor axis. This leads to sublimation occurring ≈ 0.3 au closer to the star.

where a_0 is the initial semimajor axis and M_i is the stellar mass at each time step i . The equilibrium surface temperature of the planetesimal, T_i changes due to orbital evolution and increased stellar luminosity, L_i :

$$T_i = \left(\frac{L_i(1-A)}{16\pi\epsilon\sigma(a_i - R_i)^2} \right)^{1/4} \quad (3)$$

where A and ϵ is the albedo and emissivity of the planetesimal, σ is the Stefan-Boltzmann constant, and R_i is the stellar radius. Removal of material from the planetesimal surface is governed by the Jeans escape parameter, which is the ratio of the escape velocity, v_{esc} to the thermal velocity, v_{therm} :

$$\lambda = \left(\frac{v_{\text{esc}}}{v_{\text{therm}}} \right)^2 = \frac{Gm_i\mu}{k_B T_i r_i} \quad (4)$$

where m_i and r_i are the instantaneous mass and radius of the planetesimal, μ the molecular mass of the mineral, G the gravitational constant, and k_B the Boltzmann constant. Material is removed when $\lambda \lesssim 1$.

We consider two planetesimal structures. The first is a rocky planetesimal, comprised of an Fe core accounting for 25 per cent of the mass, surrounded by an enstatite (MgSiO_3) mantle which is the remainder of the mass⁷. We assume $A = 0.1$ and $\epsilon = 0.9$ similar to that of Ceres (Li et al. 2006). The mass loss rate per unit area for a given mineral is (Vanderburg et al. 2015):

$$J = \alpha P_{\text{vap}} \sqrt{\frac{\mu}{2\pi k_B T_i}} \text{ [g s}^{-1} \text{ cm}^{-2}] \quad (5)$$

where k_B is the Boltzmann constant and α is the sticking coefficient. We take $\alpha = 0.1$ for enstatite and $\alpha = 1$ for iron (van Lieshout et al. 2014). P_{vap} is the vapour pressure, which is dependent on type of mineral and temperature:

$$P_{\text{vap}} = 0.1 e^{-\mathcal{A}/T + \mathcal{B}} \text{ [Pa]} \quad (6)$$

with values for enstatite of $\mathcal{A} = 68\,908$ and $\mathcal{B} = 38.1$ (van Lieshout et al. 2014).

The second planetesimal we consider is a rocky enstatite core which makes up 25 per cent of the mass surrounded by an icy shell of entirely H_2O which is the remaining 75 per cent of the mass. We take $A = 0.5$ and $\epsilon = 0.5$ due to increased reflection from the icy surface, which is typical of Kuiper Belt objects (Johnson et al. 2015). For ice, we use a sticking coefficient of $\alpha = 1$ (Schaller & Brown 2007) and values for temperature-dependent vapour pressure P_{vap} ice using:

$$P_{\text{vap}} = 10^{\mathcal{A} + \mathcal{B}/T + C \log T + \mathcal{D}T} \text{ [Pa]} \quad (7)$$

where the constants for H_2O ice are $\mathcal{A} = 4.07023$, $\mathcal{B} = -2484.986$, $C = 3.56654$, and $\mathcal{D} = -0.00320981$ (Huebner 2006). We assume that the rotation period is short compared to time-step Δt and that the planetesimal is not tidally locked because the tide induced by the star on the planetesimal is so weak that spin-orbit synchronization cannot be reached within the planetesimal's lifetime. The mass loss per time-step is:

$$\Delta m = J 4\pi r^2 \Delta t f_{\text{esc}} \quad (8)$$

⁷ We do not consider a crust because its mass is negligible compared to the mantle.

where f_{esc} is the fraction of gas particles which can escape the gravitational potential of the planetesimal, using a Maxwell-Boltzmann distribution. This leads to a change in mass of:

$$m_{i+1} = m_i - \Delta m \quad (9)$$

As the mass and radius of the planetesimal decreases, the density will increase because the higher density core will make up a larger fraction of the body. To simplify the radius calculation, we adopt a constant mantle density of ρ , with the density of the core a factor β larger than the mantle, $\beta\rho$, where $\beta > 1$. The core mass, $m_{\text{core}} = 0.25m_0$, and radius, r_{core} , will remain constant at:

$$r_{\text{core}}^3 = \frac{3 \times 0.25m_0}{4\pi\beta\rho} = \frac{3m_0}{16\pi\beta\rho} \quad (10)$$

However, the radius of the mantle will decrease as mass is lost, $m_0 - m_i$. The change in volume can be used to calculate the new planetesimal radius:

$$\frac{m_{\text{mantle},i}}{\rho} = \frac{0.75m_0 - (m_0 - m_i)}{\rho} = \frac{4}{3}\pi(r_i^3 - r_{\text{core}}^3) \quad (11)$$

After mass loss, the radius will be:

$$r_i^3 = r_{\text{core}}^3 + \frac{3(m_i - 0.25m_0)}{4\pi\rho} = \frac{3m_0}{16\pi\beta\rho} + \frac{3(m_i - 0.25m_0)}{4\pi\rho} \quad (12)$$

which gives:

$$r_i = \left(\frac{(3 - 3\beta)m_0 + 12\beta m_i}{16\pi\beta\rho} \right)^{1/3} \quad (13)$$

For the rocky case, the Fe-Ni alloy in the core is approximately twice the density of enstatite in the mantle so we take $\beta = 2$. For the icy case, water ice is three times less dense than enstatite so we take $\beta = 3$. To calculate the density of the mantle, ρ , we use Eq. 13 with $m_0 = M_{\text{Ceres}}$, $r_i = R_{\text{Ceres}}$, and $m_i = m_0$. For $\beta = 2$, we calculate $\rho = 1850 \text{ kg m}^{-3}$ and for $\beta = 3$ we find $\rho = 1760 \text{ kg m}^{-3}$. This is not the measured density of enstatite or ice, because this planetesimal would not be solid rock. This density is comparable to the measured density of Ceres (Park et al. 2020), but does not match exactly because Ceres is a much more complex body than this simple two layer model.

We record the total mass loss at the end of the simulation as a fraction of the initial mass. The simulations are run with a grid of planetesimals with initial masses $m_{i=0} = 0.01, 0.1, 1 M_{\text{Ceres}}$, and initial orbits spanning $a_0 = 1.80 - 3.54 \text{ au}$ in 0.01 au steps for the rocky case and $a_0 = 68 - 250 \text{ au}$ in 2 au steps for the icy case. As the Jeans escape parameter λ scales with planetesimal mass, removal of material is precluded for planetesimals with masses more than a few M_{Ceres} . The internal energy of small planetesimals is incapable of inducing rock-metal differentiation, as shown by bodies in the Solar System (Corry et al. 2021). We therefore do not consider objects with masses $< 0.01 M_{\text{Ceres}}$ (corresponding to a radius of $\lesssim 100 \text{ km}$).

The results of our simulations are shown in Fig. 5, with the sublimation of a rocky and icy mantle in the top and bottom panels respectively. For the rocky (icy) mantle, the entire layer is sublimated within $\approx 2 \text{ au}$ ($\approx 80 \text{ au}$), with smaller planetesimals less resistant to sublimation. Higher mass stars can strip planetary mantles at greater semimajor axes. For all combinations of host star and planetesimal mass, there is negligible rocky (icy) mantle loss exterior to $\approx 3 \text{ au}$ ($\approx 200 \text{ au}$). There exists a range of semimajor axes where partial mantle loss occurs. If a planetesimal belt overlaps with this region,

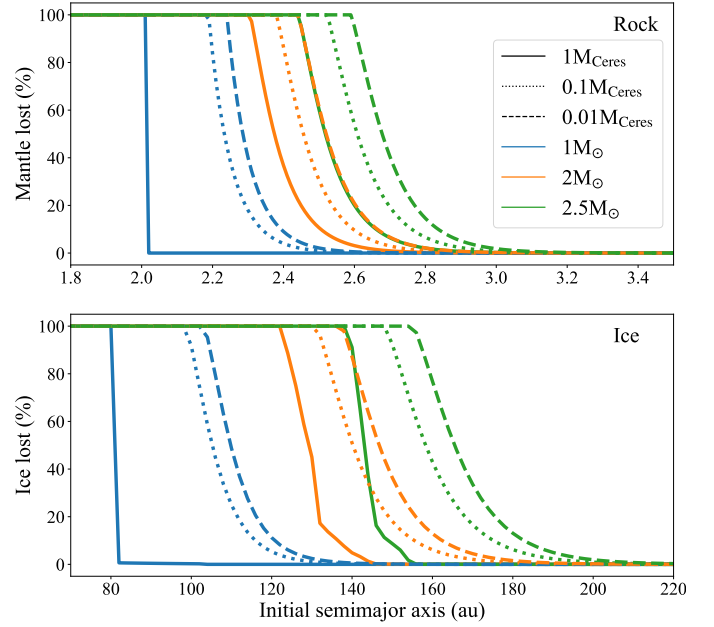


Figure 5. The percentage of mantle lost by a planetesimal with masses $m_{i=0} = 1 M_{\text{Ceres}}, 0.1 M_{\text{Ceres}}, 0.01 M_{\text{Ceres}}$ (solid, dotted, and dashed lines respectively) during post-main sequence evolution as a function of initial semimajor axis for stars of initial masses $M_0 = 1 M_{\odot}, 2 M_{\odot},$ and $2.5 M_{\odot}$ (blue, orange, green respectively). The top panel considers a rocky MgSiO_3 mantle whereas the bottom panel considers an icy H_2O mantle.

it would serve as a reservoir of objects undergoing this process. This mantle loss means that the sample of objects accreting onto white dwarfs are more core-rich and volatile-poor than their ancestors on the main sequence phase. Malamud & Perets (2016) considers a planetesimal with aqueous rock and interior ice and finds that this form of ice can survive closer to the star. In our simulation, we only considered surface ice and found that it is completely sublimated at close distances.

5 DISCUSSION

We assume that the photospheric debris in these three white dwarfs originates from a single planetesimal. Simulations of scattering events demonstrate that debris discs will be disrupted by incoming planetesimals, meaning that at any one time, the debris disc will consist of a single object (Jura 2008; Mustill et al. 2018). The atmosphere will have no record of previous material accreted more than ≈ 10 sinking timescales (approximately several months).

We assume that because we detect the major rock-forming elements O, Mg, Si, and Fe, that the total measured accretion rate is within a few per cent of the true value which allows us to compute mass fractions for each metal, listed along with their errors in Table 5 and illustrated in Fig. 6, with bulk Earth for comparison (McDonough 2000). The errors are calculated using a Monte Carlo approach, where we construct Gaussian distributions centred on the metal accretion rates and with a width of their respective error, then randomly select a set of values. We calculate the mass fraction, then repeat this 10^5 times and take the mean and standard deviation as the final result. This approach is used for all further calculations in this paper.

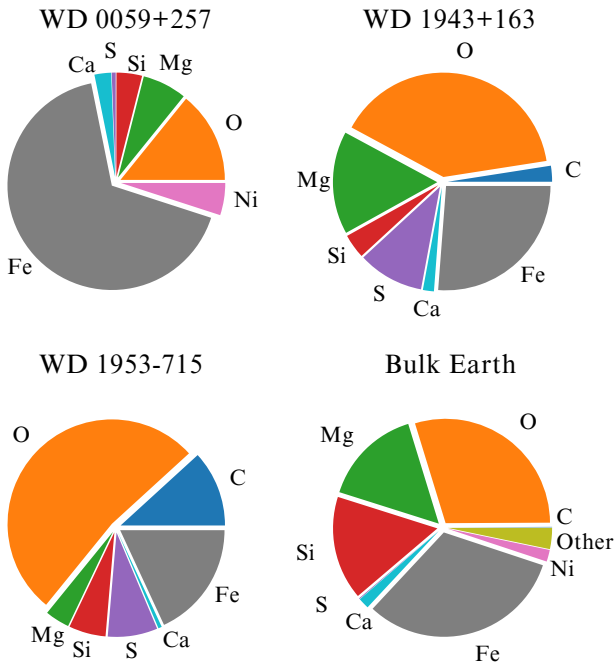


Figure 6. Mass fractions of C, O, Mg, Si, S, Ca, Fe and Ni in the debris accreted by the three white dwarfs. The corresponding mass fraction within the bulk Earth (McDonough 2000) are shown as a comparison, with “Other” representing the mass fraction of the additional elements in the bulk Earth not detected in the white dwarfs.

Table 5. Metal mass fractions of the accreted material for each white dwarf.

Z	Mass fraction (%)			
	WD 0059+257	WD 1943+163	WD 1953–715	Bulk Earth
C		2.5 ± 1.0	11.9 ± 4.9	0.07
O	14.1 ± 5.2	39.6 ± 8.6	52.2 ± 11.6	29.7
Mg	6.8 ± 2.7	15.8 ± 5.0	3.8 ± 1.6	15.4
Si	4.2 ± 3.0	3.8 ± 1.1	5.7 ± 2.1	16.1
S	0.6 ± 0.4	10.3 ± 5.7	7.7 ± 4.2	0.1
Ca	2.6 ± 1.3	1.7 ± 0.8	0.65 ± 0.3	1.7
Fe	66.8 ± 9.0	26.4 ± 8.2	18.0 ± 7.5	31.9
Ni	4.9 ± 2.9			1.8

5.1 O budget

All white dwarfs studied in this paper have detections of O, which allows us to calculate their O budget, O_{bgt} , following the prescription of Klein et al. (2010). We assume a bulk Earth-like oxidation state where the metals are found in the form of the oxides FeO, MgO, SiO₂, CaO, and NiO. We can hence write all metal oxides in the form $Z_{a(Z)}O_{b(Z)}$, and O_{bgt} then becomes

$$O_{\text{bgt}} = \sum_Z \frac{a(Z) \dot{M}_Z A(O)}{b(Z) \dot{M}_O A(Z)} \quad (14)$$

where \dot{M} and A is the accretion rate and atomic mass and the subscript denotes the metal. Strictly speaking $O_{\text{bgt}} > 1$ is physically impossible as there is not enough O to account for all the metals in the white dwarf atmosphere. However, we do not know the oxidation state of Fe, which could even be accreted in fully metallic form. FeO and Fe₂O₃ are possible states in the Earth’s crust, with the latter one dominating. However, the state of Fe in the deeper layers is not well established, with volcanic studies suggesting FeO is more common (Basaltic Volcanism Study Project 1981; Workman & Hart 2005)

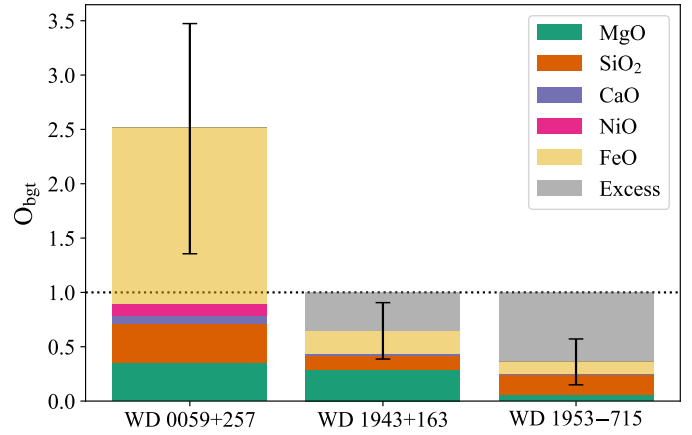


Figure 7. The O_{bgt} for the debris at the three white dwarfs studied, assuming metals are in the oxides of MgO, SiO₂, CaO, NiO, and FeO. We allow the fraction of fully metallic and fully oxidised. The error bars show the total error on the O_{bgt} . The relative error for all three systems is similar, but WD 0059+257 has the largest O_{bgt} and hence has the largest absolute error.

whereas magnetic studies support a substantial fraction of Fe₂O₃ (Kupenko et al. 2019). We make a simplifying assumption that FeO is the only oxidised form of Fe and keep the contribution of FeO to the O_{bgt} as a free parameter. In the case of a balanced $O_{\text{bgt}} = 1$ all O can be accounted for by the accreted metal oxides. $O_{\text{bgt}} < 1$ suggests an O excess, which requires an additional carrier of O in the accreted debris. The most plausible nature of that extra O carrier is water, H₂O. The O_{bgt} for each of the white dwarfs is shown in Fig. 7. For WD 0059+257, most of Fe must be metallic to be consistent with $O_{\text{bgt}} \leq 1$, implying the accreted body was in a reduced state. WD 1943+163 and WD 1953–715 have O excesses, so likely contain ice.

5.2 Comparison to Solar System objects

To determine the nature of the material accreted by these three white dwarfs we use a χ^2 minimisation approach to find the most similar Solar System object, using the method outlined in Xu et al. (2013). We take abundances relative to the combination of the four most common rock-forming elements, O, Mg, Si, and Fe, in order to reduce the sensitivity to the abundance measurement of a single metal:

$$\chi^2 = \frac{1}{N_Z} \sum \left[\frac{\frac{\dot{M}_Z/A_Z}{\dot{M}_O/A_O + \dot{M}_{\text{Mg}}/A_{\text{Mg}} + \dot{M}_{\text{Si}}/A_{\text{Si}} + \dot{M}_{\text{Fe}}/A_{\text{Fe}}} - \left(\frac{Z}{\text{O+Mg+Si+Fe}} \right)_{\text{met}}}{\dot{M}_{Z,\text{err}}^2 + \dot{M}_{O,\text{err}}^2 + \dot{M}_{\text{Mg},\text{err}}^2 + \dot{M}_{\text{Si},\text{err}}^2 + \dot{M}_{\text{Fe},\text{err}}^2} \right]^2 \quad (15)$$

where N_Z is the number of detected metals, the subscript “met” denotes the abundance of an individual meteorite, and the subscript “err” denotes the error in the accretion rate.

The material accreted by WD 0059+257 is most similar to pallasites and mesosiderites (Nittler et al. 2004), both of which are stony-iron meteorites with traces of Fe-Ni alloy. The core Earth composition of McDonough (2000) does not contain data on O or Mg and hence was not fitted in our χ^2 minimisation, but we do note that the composition of WD 0059+257 closely matches core Earth in the left panel of Fig. 8. For WD 1943+163, we find the ten best-fitting Solar System objects (Lodders 2003; Nittler et al. 2004) are all

carbonaceous chondrites, with the closest match from the meteorite Tonk, which we illustrate in Fig. 8. The best-fitting Solar system object for WD 1953–715 is with a solar composition, due to the high abundance of volatiles, which are depleted in most rocky objects.

We now discuss each object individually using the O budgets we have calculated and by comparing to Solar System objects. We also explore whether mantle sublimation has affected the composition of each accreted object.

5.3 WD 0059+257

The planetary debris around WD 0059+257 is extraordinarily rich in Fe and Ni, which make up a combined 71.8 ± 7.9 per cent of its mass. Fe and Ni are siderophile elements which preferentially partition into the core during differentiation. Several other white dwarfs share similar siderophile enhancements (GALEX J193156.8+01174, Melis et al. 2011; PG 0843+516, Gänsicke et al. 2012; Ton 345, Wilson et al. 2015; NLTT 888, Kawka & Vennes 2016; SDSS J074153.45+314620.4 and SDSS J082303.82+054656.1, Hollands et al. 2018), with the standard interpretation being that the debris progenitor is a fragment of the core of a chemically differentiated planetesimal. Using PYLLUTEDWD⁸ (Harrison et al. 2018, 2021; Buchan et al. 2022), we find a core mass fraction of 69 per cent, over double that of Earth’s at 32.5 per cent and comparable to Mercury’s of 60–70 per cent (Hauck et al. 2013). Mercury is a very reduced object and contains a large mass fraction of Fe, predicted to be due to collisions having stripped the mantle (Benz et al. 1988). The best-fitting meteorite family to the debris, mesosiderites, are speculated to originate from the M-type asteroid Psyche (Davis et al. 1999). This object is hypothesised to be an exposed planetary core (Elkins-Tanton et al. 2022), which could have lost its mantle due to a violent collision with another large object (Asphaug et al. 2011; Asphaug 2017).

However, as discussed in Section 4, a differentiated object with a mass of $M \lesssim 1 M_{\text{Ceres}}$ can lose a portion of its mantle during post-main sequence evolution, making the remaining planetesimal core-rich. With a progenitor mass of $M \lesssim 1 M_{\odot}$ ⁹, a planetesimal with an initial semimajor axis in the region of $2.2 \lesssim a_0 \lesssim 2.6$ au could have undergone mantle sublimation. The Fe-rich planetesimals accreting onto GALEX J193156.8+011745 (Melis et al. 2011) and Ton 345 (Wilson et al. 2015) have compositions that are consistent with a bulk Earth-like differentiated object with a fraction of the mantle removed. Using the prescription from Melis et al. (2011) and compositions from McDonough (2000), we assume that the core consists of Fe and Ni whereas the mantle contains O, Mg, Si, Ca, Fe, and traces of S and Ni. We gradually remove the mantle so that the composition becomes more core-rich, finding that the best fit is to an object with 65 per cent of the mantle removed, which is shown in Fig. 9.

The possible oxidation state of the parent body suggests that a large fraction of Fe must be in its metallic form, as shown by Fig. 7. The Earth’s core consists mainly of a reduced Fe-Ni alloy with $\log(\text{Ni}/\text{Fe}) = -1.235$ (McDonough 2000). The planetesimal accreted by WD 0059+257 has a similar ratio of $\log(\text{Ni}/\text{Fe}) = -1.2 \pm 0.3$. Earth’s core must also contain a lighter element because the inferred density of the core is 10 per cent lower than

pure Fe-Ni alloy. The light element is commonly predicted to be either O, Si or S (Birch 1952, 1964; Dreibus & Palme 1996). In the object accreted by WD 0059+257, O and Si have abundances of $\log(\text{O}/\text{Mg}) = 0.50 \pm 0.20$ and $\log(\text{Si}/\text{Mg}) = -0.35 \pm 0.28$, similar to that of the Earth’s mantle of $\log(\text{O}/\text{Mg}) = 0.468$ and $\log(\text{Si}/\text{Mg}) = -0.098$. Assuming that this differentiated body underwent mantle stripping similar to the toy model illustrated in Fig. 9, this means that O and Si have abundances consistent with being only present in the mantle of this model. However, S is enhanced at $\log(\text{S}/\text{Mg}) = -1.23 \pm 0.32$ with respect to Earth’s mantle at $\log(\text{S}/\text{Mg}) = -3.08$. So, assuming this toy model, S must also be present within the core of the accreted body. We caveat this with the S detection having a large error and the simplicity of our toy model for the planetesimal, but we also note that PG 0843+516 accretes core-rich material, as well as noticeable amounts of S (Gänsicke et al. 2012).

Whereas the presence of a light element in the core of the Earth is undisputed, determining its nature has proven extraordinarily difficult, as it is impossible to measure the composition of the Earth’s core directly. Whereas the number of white dwarfs accreting core-rich objects is still relatively small (left panel of Fig. 8), the identification of several 100 000 white dwarf candidates using data from the Gaia mission (Gentile Fusillo et al. 2021) and the ongoing efforts in spectroscopic follow-up (e.g. Manser et al. 2024) demonstrate the potential of unambiguously identifying light elements present within differentiated planetary cores from studying debris-accretion white dwarfs.

5.4 WD 1943+163

Distinguishing between bulk Earth and chondritic material is possible through observations of the volatile elements C and S in the FUV. Although the refractory elements observed in WD 1943+163 agree with the composition of the bulk Earth (Figs. 6, 8), the enhanced volatile abundances from C, O, and S suggest that the accreted material is a carbonaceous chondrite, see the right panel of Fig. 8.

Carbonaceous chondrites are the primitive building blocks of the Solar System (Alexander et al. 2012), and have not undergone melting or differentiation. They are among the most C-rich objects known (Lodders 2003) and are predicted to have formed in the outer Solar System (Wood 2005; Warren 2011). The abundances of volatiles within a planetary object are expected to increase with increasing distance from the host star (Larimer 1967; Lewis 1972) due to lower temperatures during planet formation because of the reduced levels of volatile sublimation. The volatile enhancement in the planetesimal accreted by WD 1943+163 therefore suggests that it formed at a large separation from its host star and that it did not undergo incomplete accretion (Albarède 2009) or volatile outgassing like Earth did (Thompson et al. 2021, 2023). The large radial distance from the star is further supported by the fact that it did not lose volatiles during post-main sequence evolution (Malamud & Perets 2016).

In the Solar System, carbonaceous chondrites contain carbonates and minerals modified by water (Bischoff 1998; Alexander et al. 2015). Examining the O_{bgt} for WD 1943+163 in Fig. 7, we find that even under the assumption that all Fe is in the form of FeO (the mass fraction of metallic Fe in carbonaceous chondrites is low), there is a slight O excess, which can be interpreted as evidence for water. However, the large mass fraction of C means that C-based ice (CO or CO₂) could be present instead of water ice.

Another striking feature of the planetesimal accreted by WD 1943+163, illustrated in the top right panel of Fig. 6 and the centre panel of Fig. 8, is a significant Si depletion. Both chondritic and

⁸ https://github.com/andrewbuchan4/PyllutedWD_Public

⁹ The low mass of WD 0059+257 is in the poorly constrained region of the initial-to-final-mass relation (Heintz et al. 2022), so we can only place an upper limit on the progenitor mass (Ould Rouis et al. 2024).

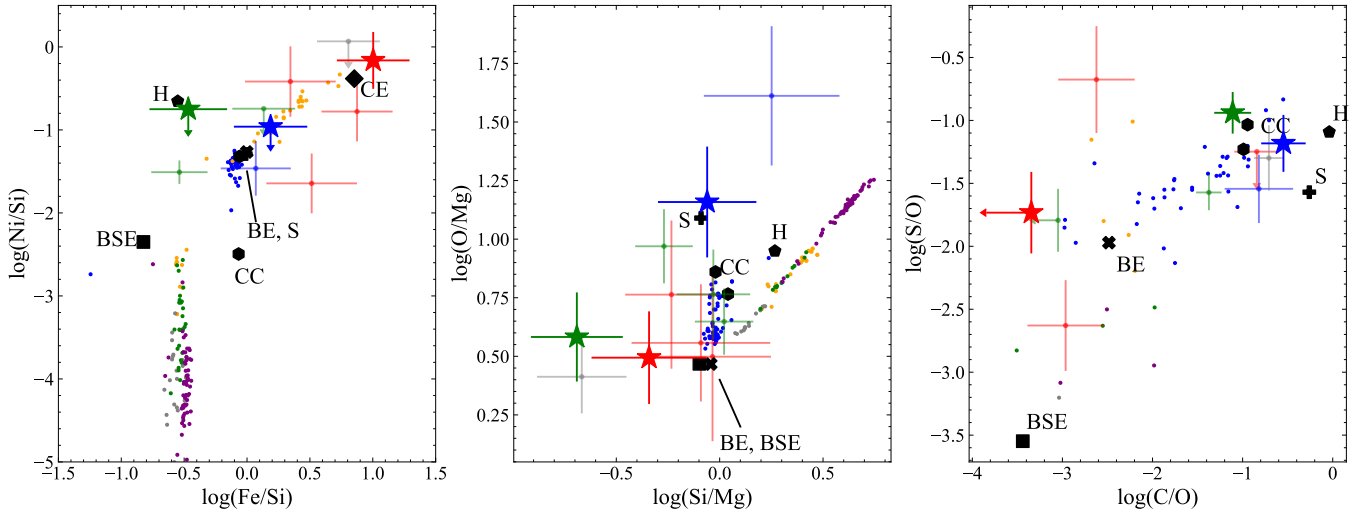


Figure 8. Number abundance ratios generated using PEWDD, with stars representing WD 0059+257 (red), WD 1943+163 (green), and WD 1953–715 (blue). For comparison, we include meteorites from [Nittler et al. \(2004\)](#) (carbonaceous chondrites: blue, mesoderites: orange, pallasites: red, diogenites: grey, howardites: green, eucrites: purple). We also show various Solar System objects including bulk Earth (BE, cross; [McDonough 2000](#)), bulk silicate Earth (BSE, square; [McDonough 2000](#)), core Earth (CE, diamond; [McDonough 2000](#)), Halley’s comet (H, pentagon; [Jessberger et al. 1988](#)), the carbonaceous chondrite Tonk (CC, hexagon; [Nittler et al. 2004](#)), and a solar composition (S, plus; [Asplund et al. 2005](#)). Using PEWDD, we identify several white dwarfs with comparable temperatures and accreting similar objects to the ones studied in this paper. Core-rich objects are shown in orange (Ton 345; [Wilson et al. 2015](#), PG 0843+516, and GALEX J193156.8+01174; [Gänsicke et al. 2012](#)), chondritic objects in purple (WD J204713.76–125908.9; [Hoskin et al. 2020](#), GD 61; [Farihi et al. 2013](#), and WD 1232+563; [Xu et al. 2019](#)), WD 1425+540 which is accreting a Kuiper Belt-like object is shown in pink ([Xu et al. 2017](#)), and G 238-44 which is thought to accrete a mixture of one core-rich and one volatile-rich object is shown in gray ([Johnson et al. 2022](#)).

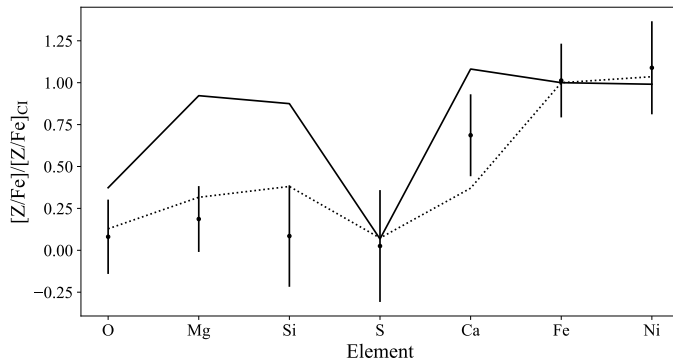


Figure 9. Abundances of the material accreted by WD 0059+257 relative to Fe and normalised to CI chondrites (black points). These are compared to a bulk Earth model (solid line) and a best-fitting model where 65 per cent of the mantle is removed (dotted line).

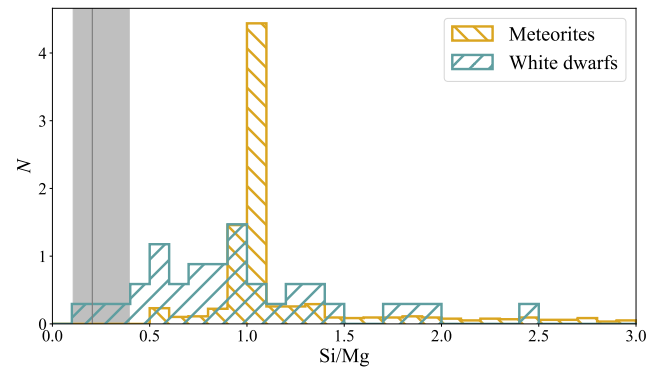


Figure 10. The distribution of Si/Mg abundances for meteorites in the Solar System ([Nittler et al. 2004](#)) and for white dwarfs in PEWDD with accretion rates for Si and Mg. The vertical line and shaded region is the Si/Mg abundance and error bounds for the material accreted by WD 1943+163.

bulk Earth material have $\text{Si}/\text{Mg} \approx 1$, whereas the material accreted by WD 1943+163 has $\text{Si}/\text{Mg} \approx 0.2$. This cannot be explained by the accretion of a differentiated body such as a mantle-rich fragment as the abundance for bulk silicate Earth is $\text{Si}/\text{Mg} \approx -0.8$ ([McDonough 2000](#)), mainly consisting of rocks with broadly equal Mg and Si abundances. Furthermore Fig. 10 illustrated that no meteorite sample (orange histogram) has an Si/Mg ratio as low as that within the object accreted by WD 1943+163. The Si discrepancy discussed in Section 3.1.4 cannot account for the observed under-abundance, as the adopted Si uncertainties already incorporate this, and a depletion remains even within error.

Using PEWDD, we select 34 white dwarfs that have Mg and Si, and show the resulting Si/Mg ratios as blue histogram in Fig. 10. This distribution, similarly to that of Solar System meteorites, peaks at approximately equal Mg and Si abundances, but has a much longer tail

towards Si-depleted objects. Three white dwarfs have Si/Mg abundances that agree with that of the object accreted by WD 1943+163: PG 1015+161 ([Gänsicke et al. 2012](#)), PG 1018+411 ([Xu et al. 2019](#)), and G 238-44 ([Johnson et al. 2022](#)). All four strongly Si-depleted white dwarfs have warm ($19000 < T_{\text{eff}} < 25000$ K) H-dominated atmospheres and were studied using FUV *HST*/COS spectroscopy. [Johnson et al. \(2022\)](#) concludes that the Si depletion of G 238-44 cannot be explained by a Si-poor host star. However, Fig. 10 shows that strong Si depletion is generally not common among debris-accreting white dwarfs, and the two other white dwarfs studied in this paper, having warm H-dominated atmospheres as well, have $\text{Si}/\text{Mg} \approx 0.5$ for WD 0059+257, and $\text{Si}/\text{Mg} \approx 1.5$ for WD 1953–715, consistent with Solar System objects. The geochemical processes that could lead to the Si-depletion detected in the four white dwarfs mentioned above is presently not clear.

5.5 WD 1953–715

Two-thirds of the mass of the object accreted by WD 1953–715 consists of the volatiles C, O, and S (bottom left panel of Fig. 6), and the best-fitting Solar System body is the Sun. Planetesimals that form within the snow line generally consist of rocky, volatile-poor material whereas objects formed further from the star, e.g. those in the Kuiper Belt, are enhanced in volatiles (Morbidei et al. 2000). Only two Kuiper Belt object (KBO) analogues have been identified accreting onto white dwarfs: WD 1425+540 (Xu et al. 2017) and G 238-44 (Johnson et al. 2022). The C/O and S/O ratios of WD 1953–715 agree with those measured in these systems, and are close to those of Halley’s comet (Jessberger et al. 1988).

We find a lower limit of an O excess of $O_{\text{bgt}} = 64 \pm 21$ per cent, which is a 3σ detection. Similar to KBOs, we assume this O is mainly in the form of H_2O (Jewitt & Luu 2004; Filacchione et al. 2016), but note that the large C mass fraction of 11.9 ± 4.9 per cent suggests C could partially be in the form of CO and CO_2 ices, but also molecules such as CH_4 , HCN, CH_3OH , or hydrocarbons (Strøm et al. 2020). A Solar System equivalent could be Ceres, which has an icy mantle and is C-rich (Marchi et al. 2019).

However, the body accreted by WD 1953–715 must have been located further out than Ceres otherwise the icy mantle would have been lost during the evolution of the host star (Fig. 5). Within the Solar System, the sublimation of H_2O of comets begins at 2.5 au from the Sun (Strøm et al. 2020), the result of which are visible as cometary tails. During the post-main sequence evolution, sublimation occurs at much larger separations (bottom panel of Fig. 5), and the region of complete ice sublimation places constraints on the initial semimajor axes of bodies with thick ice layers accreting onto white dwarfs. Although these simulations consider a simplistic two-layer model with no porosity, we can conclude that the planetesimal accreted by WD 1953–715 likely originated from ≥ 150 au the host star, which had an initial mass of $M_\star \approx 2.5M_\odot$ ¹⁰. In the context of the Solar System, this would place the body beyond the Kuiper Belt but within the inner radius of the Oort Cloud. Observations of exo-Kuiper Belts suggests that this region is well populated (Chen et al. 2006; Lawler et al. 2009; Ren et al. 2019).

The strongest evidence of WD 1425+540 and G 238-44 accreting KBO analogues is the detection of N, which is strongly depleted in most rocky objects but enhanced in KBOs (Xu et al. 2017; Johnson et al. 2022). We did not detect N in WD 1953–715 and could not place a stringent upper limit due to strong ISM line contamination, but this does not rule out a large N mass fraction. However, the necessity of ices to fulfil the O_{bgt} and the results of the simulation shown in Fig. 5 suggests that this object must have been located at a large radial distance from the host star.

The KBO that accretes onto WD 1425+540 was likely sent on to a star-grazing orbit by its wide binary companion (Xu et al. 2017). WD 1953–715 does not have a wide binary companion, and Li et al. (2022) finds that trans-Neptunian objects will only have detectable accretion rates of $10^7 - 10^8 \text{ g s}^{-1}$ for white dwarfs older than 100 Myr. WD 1953–715 is the oldest of the white dwarfs analysed in this paper with $t_{\text{cool}} = 106 \pm 4$ Myr, and a total accretion rate of $5.5 \times 10^7 \text{ g s}^{-1}$, i.e. within the predicted range. The same delivery mechanism is assumed for the KBO accreting onto G 238-44 (Johnson et al. 2022), however, there are additional dynamical pathways for Oort Cloud-analogue objects to be disrupted on to star-grazing orbits (Veras et al. 2014; Pham & Rein 2024).

6 CONCLUSIONS

Using UV and optical spectroscopy, we measured the bulk abundances of three planetesimals accreting onto white dwarfs, and we discuss their possible structures and evolution. Although the three white dwarfs studied here have similar masses and cooling ages, our analysis shows that the accreted planetesimals display a large diversity their compositions. We demonstrate that sublimation during the post-main sequence phase can alter the properties of planetesimals before they are accreted.

The planetesimal accreted by WD 0059+257 shows strong evidence of differentiation, and is among the most core-rich extrasolar planetary body identified so far. In contrast, WD 1943+163 and WD 1953–715 closely resemble carbonaceous chondrites and Kuiper-belt objects, with the former displaying a substantial level of Si depletion. The detection of volatiles (C, S) are critically important in the interpretation of the formation and structure of planetary bodies, and are only possible through FUV spectroscopy of relatively warm and young white dwarfs. The growing sample of white dwarfs observed with *HST/COS* is beginning to provide detailed statistical insight into the composition of rocky planetesimals in our solar neighbourhood.

ACKNOWLEDGEMENTS

We thank the referee for providing a detailed and constructive report. JTW wants to thank Andrew Swan, Mark Hollands, and Alexander Mustill for useful discussions regarding the interpretation of the accreted debris. This research is based on observations made with the NASA/ESA *Hubble Space Telescope* obtained from the Space Telescope Science Institute, which is operated by the Association of Universities for Research in Astronomy, Inc., under NASA contract NAS 5–26555. These observations are associated with the program 12169. Also based on observations made with ESO Telescopes at the La Silla Paranal Observatory under programme ID 091.C–0670. This research received funding from the European Research Council under the European Union’s Horizon 2020 research and innovation programme number 101020057 (JTW, BTG, SS). This work has made use of data from the European Space Agency (ESA) mission *Gaia* (<https://www.cosmos.esa.int/gaia>), processed by the Gaia Data Processing and Analysis Consortium (DPAC, <https://www.cosmos.esa.int/web/gaia/dpac/consortium>). Funding for the DPAC has been provided by national institutions, in particular the institutions participating in the Gaia Multilateral Agreement. This research made use of Astropy¹¹, a community-developed core Python package for Astronomy (Astropy Collaboration et al. 2013, 2018), scipy (Virtanen et al. 2020) and specutils (Earl et al. 2023).

DATA AVAILABILITY

The *HST/COS* data used in this paper is available in the MAST archive under the program ID 12169. The VLT/UVES data is available in the ESO archive under program ID 091.C–0670.

REFERENCES

Albarède F., 2009, *Nature*, 461, 1227

¹⁰ We use the initial-to-final mass relation from Cummings et al. (2018).

¹¹ <https://www.astropy.org/>

- Alexander C. M. O., Bowden R., Fogel M. L., Howard K. T., Herd C. D. K., Nittler L. R., 2012, *Science*, **337**, 721
- Alexander C. M. O., Bowden R., Fogel M. L., Howard K. T., 2015, *M&PS*, **50**, 810
- Althaus L. G., Miller Bertolami M. M., Córscico A. H., 2013, *A&A*, **557**, A19
- Asphaug E., 2017, in Elkins-Tanton L. T., Weiss B. P., eds., *Planetesimals: Early Differentiation and Consequences for Planets*. Cambridge University Press, pp 7–37, doi:10.1017/9781316339794.002
- Asphaug E., Jutzi M., Movshovitz N., 2011, *Earth and Planetary Science Letters*, **308**, 369
- Asplund M., Grevesse N., Sauval A. J., 2005, in Barnes Thomas G. I., Bash F. N., eds, *Astronomical Society of the Pacific Conference Series Vol. 336, Cosmic Abundances as Records of Stellar Evolution and Nucleosynthesis*. p. 25
- Astropy Collaboration et al., 2013, *A&A*, **558**, A33
- Astropy Collaboration et al., 2018, *AJ*, **156**, 123
- Basaltic Volcanism Study Project 1981, *Basaltic Volcanism on the Terrestrial Planets*. Pergamon Press, Inc, New York
- Bédard A., Bergeron P., Brassard P., Fontaine G., 2020, *ApJ*, **901**, 93
- Benz W., Slattery W. L., Cameron A. G. W., 1988, *Icarus*, **74**, 516
- Birch F., 1952, *J. Geophys. Res.*, **57**, 227
- Birch F., 1964, *J. Geophys. Res.*, **69**, 4377
- Bischoff A., 1998, *M&PS*, **33**, 1113
- Bonsor A., Farihi J., Wyatt M. C., van Lieshout R., 2017, *MNRAS*, **468**, 154
- Bonsor A., Carter P. J., Hollands M., Gänsicke B. T., Leinhardt Z., Harrison J. H. D., 2020, *MNRAS*, **492**, 2683
- Bourrier V., et al., 2018, *A&A*, **615**, A117
- Buchan A. M., Bonsor A., Shorttle O., Wade J., Harrison J., Noack L., Koester D., 2022, *MNRAS*, **510**, 3512
- Camisassa M. E., Althaus L. G., Córscico A. H., Vinyoles N., Serenelli A. M., Isern J., Miller Bertolami M. M., García-Berro E., 2016, *ApJ*, **823**, 158
- Camisassa M. E., et al., 2019, *A&A*, **625**, A87
- Carry B., et al., 2021, *A&A*, **650**, A129
- Chen C. H., et al., 2006, *ApJS*, **166**, 351
- Choi J., Dotter A., Conroy C., Cantiello M., Paxton B., Johnson B. D., 2016, *ApJ*, **823**, 102
- Cummings J. D., Kalirai J. S., Tremblay P. E., Ramirez-Ruiz E., Choi J., 2018, *ApJ*, **866**, 21
- Cunningham T., et al., 2021, *MNRAS*, **503**, 1646
- Davis D. R., Farinella P., Marzari F., 1999, *Icarus*, **137**, 140
- Dekker H., D’Odorico S., Kaufér A., Delabre B., Kotzowski H., 2000, in Iye M., Moorwood A. F., eds, *Society of Photo-Optical Instrumentation Engineers (SPIE) Conference Series Vol. 4008, Optical and IR Telescope Instrumentation and Detectors*. pp 534–545, doi:10.1117/12.395512
- Dorn C., Khan A., Heng K., Connolly J. A. D., Alibert Y., Benz W., Tackley P., 2015, *A&A*, **577**, A83
- Dotter A., 2016, *ApJS*, **222**, 8
- Doyle A. E., et al., 2023, *ApJ*, **950**, 93
- Dreibus G., Palme H., 1996, *Geochimica Cosmochimica Acta*, **60**, 1125
- Earl N., et al., 2023, *astropy/specutils*: v1.10.0, doi:10.5281/zenodo.7803739
- Elkins-Tanton L. T., et al., 2022, *Space Sci. Rev.*, **218**, 17
- Farihi J., Gänsicke B. T., Koester D., 2013, *Science*, **342**, 218
- Filacchione G., et al., 2016, *Nature*, **529**, 368
- Freudling W., Romaniello M., Bramich D. M., Ballester P., Forchi V., García-Dabó C. E., Moehler S., Neeser M. J., 2013, *A&A*, **559**, A96
- Gänsicke B. T., Marsh T. R., Southworth J., Rebassa-Mansergas A., 2006, *Science*, **314**, 1908
- Gänsicke B. T., Koester D., Farihi J., Girven J., Parsons S. G., Breedt E., 2012, *MNRAS*, **424**, 333
- Gentile Fusillo N. P., et al., 2021, *MNRAS*, **508**, 3877
- Girven J., Brinkworth C. S., Farihi J., Gänsicke B. T., Hoard D. W., Marsh T. R., Koester D., 2012, *ApJ*, **749**, 154
- Green J. C., et al., 2012, *ApJ*, **744**, 60
- Harrison J. H. D., Bonsor A., Madhusudhan N., 2018, *MNRAS*, **479**, 3814
- Harrison J. H. D., Bonsor A., Kama M., Buchan A. M., Blouin S., Koester D., 2021, *MNRAS*, **504**, 2853
- Hauk S. A., et al., 2013, *Journal of Geophysical Research (Planets)*, **118**, 1204
- Heintz T. M., Hermes J. J., El-Badry K., Walsh C., van Saders J. L., Fields C. E., Koester D., 2022, *ApJ*, **934**, 148
- Hollands M. A., Gänsicke B. T., Koester D., 2018, *MNRAS*, **477**, 93
- Hollands M. A., et al., 2020, *Nature Astronomy*, **4**, 663
- Hollands M. A., Tremblay P.-E., Gänsicke B. T., Koester D., Gentile-Fusillo N. P., 2021, *Nature Astronomy*, **5**, 451
- Hoskin M. J., et al., 2020, *MNRAS*, **499**, 171
- Huebner ed. 2006, *Heat and Gas Diffusion in Comet Nuclei*
- Jessberger E. K., Christoforidis A., Kissel J., 1988, *Nature*, **332**, 691
- Jewitt D. C., Luu J., 2004, *Nature*, **432**, 731
- Johnson R. E., Oza A., Young L. A., Volkov A. N., Schmidt C., 2015, *ApJ*, **809**, 43
- Johnson T. M., Klein B. L., Koester D., Melis C., Zuckerman B., Jura M., 2022, *ApJ*, **941**, 113
- Jura M., 2008, *AJ*, **135**, 1785
- Kausch W., et al., 2015, *A&A*, **576**, A78
- Kawka A., Vennes S., 2016, *MNRAS*, **458**, 325
- Klein B., Jura M., Koester D., Zuckerman B., Melis C., 2010, *ApJ*, **709**, 950
- Koester D., 2009, *A&A*, **498**, 517
- Koester D., 2010, *Mem. Soc. Astron. Italiana*, **81**, 921
- Koester D., Gänsicke B. T., Farihi J., 2014, *A&A*, **566**, A34
- Koester D., Kepler S. O., Irwin A. W., 2020, *A&A*, **635**, A103
- Kupenko I., et al., 2019, *Nature*, **570**, 1020
- Larimer J. W., 1967, *Geochimica Cosmochimica Acta*, **31**, 1215
- Lawler S. M., et al., 2009, *ApJ*, **705**, 89
- Lewis J. S., 1972, *Earth and Planetary Science Letters*, **15**, 286
- Li J.-Y., McFadden L. A., Parker J. W., Young E. F., Stern S. A., Thomas P. C., Russell C. T., Sykes M. V., 2006, *Icarus*, **182**, 143
- Li D., Mustill A. J., Davies M. B., 2022, *ApJ*, **924**, 61
- Li Y., Bonsor A., Shorttle O., 2024, *MNRAS*, **527**, 1014
- Lodders K., 2003, *ApJ*, **591**, 1220
- Malamud U., Perets H. B., 2016, *ApJ*, **832**, 160
- Malamut C., Redfield S., Linsky J. L., Wood B. E., Ayres T. R., 2014, *ApJ*, **787**, 75
- Manser C. J., et al., 2024, *MNRAS*, **535**, 254
- Marchi S., et al., 2019, *Nature Astronomy*, **3**, 140
- McDonough W., 2000, *Earthquake thermodynamics and phase transformation in the earth’s interior*. Elsevier Science Academic Press
- Melis C., Farihi J., Dufour P., Zuckerman B., Burgasser A. J., Bergeron P., Bochanski J., Simcoe R., 2011, *ApJ*, **732**, 90
- Morbidelli A., Chambers J., Lunine J. I., Petit J. M., Robert F., Valsecchi G. B., Cyr K. E., 2000, *M&PS*, **35**, 1309
- Mustill A. J., Villaver E., Veras D., Gänsicke B. T., Bonsor A., 2018, *MNRAS*, **476**, 3939
- Nittler L. R., McCoy T. J., Clark P. E., Murphy M. E., Trombka J. I., Jarosewich E., 2004, *Antarctic Meteorite Research*, **17**, 231
- Ould Rouis L. B., et al., 2024, *ApJ*, **976**, 156
- Park R. S., et al., 2020, *Nature Astronomy*, **4**, 748
- Pathak P., Blouin S., Herwig F., 2024, *arXiv e-prints*, p. arXiv:2410.14014
- Paxton B., Bildsten L., Dotter A., Herwig F., Lesaffre P., Timmes F., 2011, *ApJS*, **192**, 3
- Paxton B., et al., 2013, *ApJS*, **208**, 4
- Paxton B., et al., 2015, *ApJS*, **220**, 15
- Paxton B., et al., 2018, *ApJS*, **234**, 34
- Pham D., Rein H., 2024, *MNRAS*, **530**, 2526
- Redfield S., Linsky J. L., 2004, *ApJ*, **613**, 1004
- Ren B., et al., 2019, *ApJ*, **882**, 64
- Rocchetto M., Farihi J., Gänsicke B. T., Bergfors C., 2015, *MNRAS*, **449**, 574
- Rogers L. K., et al., 2024, *MNRAS*, **527**, 6038
- Sahu S., et al., 2023, *MNRAS*, **526**, 5800
- Schaller E. L., Brown M. E., 2007, *ApJ*, **659**, L61
- Schatzman E., 1949, *ApJ*, **110**, 261
- Smette A., et al., 2015, *A&A*, **576**, A77
- Strøm P. A., et al., 2020, *PASP*, **132**, 101001
- Swan A., Farihi J., Koester D., Hollands M., Parsons S., Cauley P. W., Redfield S., Gänsicke B. T., 2019, *MNRAS*, **490**, 202

Swan A., Farihi J., Melis C., Dufour P., Desch S. J., Koester D., Guo J., 2023, *MNRAS*, **526**, 3815

Thompson M. A., Telus M., Schaefer L., Fortney J. J., Joshi T., Lederman D., 2021, *Nature Astronomy*, **5**, 575

Thompson M. A., Telus M., Edwards G. H., Schaefer L., Dhaliwal J., Dreyer B., Fortney J. J., Kim K., 2023, *PSJ*, **4**, 185

Valencia D., O'Connell R. J., Sasselov D., 2006, *Icarus*, **181**, 545

Vanderburg A., et al., 2015, *Nature*, **526**, 546

Veras D., Shannon A., Gänsicke B. T., 2014, *MNRAS*, **445**, 4175

Virtanen P., et al., 2020, *scipy/scipy: SciPy 1.5.3*, doi:10.5281/zenodo.4100507

Warren P. H., 2011, *Earth and Planetary Science Letters*, **311**, 93

Williams J. T., Gänsicke B. T., Swan A., O'Brien M. W., Izquierdo P., Cutolo A. M., Cunningham T., 2024, *A&A*, **691**, A352

Wilson D. J., Gänsicke B. T., Koester D., Toloza O., Pala A. F., Breedt E., Parsons S. G., 2015, *MNRAS*, **451**, 3237

Wilson D. J., Gänsicke B. T., Farihi J., Koester D., 2016, *MNRAS*, **459**, 3282

Wood J. A., 2005, in Krot A. N., Scott E. R. D., Reipurth B., eds, *Astronomical Society of the Pacific Conference Series Vol. 341, Chondrites and the Protoplanetary Disk*. p. 953

Workman R. K., Hart S. R., 2005, *Earth and Planetary Science Letters*, **231**, 53

Xu S., Jura M., Klein B., Koester D., Zuckerman B., 2013, *ApJ*, **766**, 132

Xu S., Jura M., Koester D., Klein B., Zuckerman B., 2014, *ApJ*, **783**, 79

Xu S., Zuckerman B., Dufour P., Young E. D., Klein B., Jura M., 2017, *ApJ*, **836**, L7

Xu S., Dufour P., Klein B., Melis C., Monson N. N., Zuckerman B., Young E. D., Jura M. A., 2019, *AJ*, **158**, 242

Zuckerman B., Koester D., Melis C., Hansen B. M., Jura M., 2007, *ApJ*, **671**, 872

Zuckerman B., Koester D., Dufour P., Melis C., Klein B., Jura M., 2011, *ApJ*, **739**, 101

van Lieshout R., Min M., Dominik C., 2014, *A&A*, **572**, A76

APPENDIX A: LINE LIST

This paper has been typeset from a $\text{\TeX}/\text{\LaTeX}$ file prepared by the author.

Table A1. The wavelengths of absorption features that can be found in COS or UVES spectra. Those in italics are contaminated by ISM lines or airglow, which had to be corrected for. The lines in bold were those used in computing the number abundances. For upper limits, the line that gave the tightest constraint is in bold.

Ion	Vacuum Wavelengths (Å)
C I	1158.019,1193.009,1193.240,1261.552,1277.245,1277.282,1277.550,1277.723,1280.333,1329.578,1355.844,1463.336,1560.310,1560.683,1561.438,1656.266,1656.928,1657.008,1657.380,1657.907,1658.122,1930.905
C II	1323.906,1323.951, 1334.532 , 1335.663 , 1335.708
C III	1174.930 , 1175.260 , 1175.590 , 1175.710 , 1175.987 , 1176.370
N I	<i>1134.165</i> , <i>1134.415</i> , <i>1134.980</i> ,1167.448,1168.536,1176.510, 1199.550 , 1200.223 , 1200.710 ,1243.179,1243.306,1310.540,1319.676,1411.948
O I	1152.150 , 1302.170 , 1304.860 , 1306.030
Mg II	1369.423, 4482.383 , 4482.403 , 4482.583 ,7879.221,7898.539,8236.899
Al II	1189.185,1190.046,1190.051,1191.808,1191.814,1210.082,1211.899
Al III	1379.670 , 1384.132
Si II	1190.416 , 1193.290 , 1194.500 , 1197.394 ,1224.245,1226.798,1226.979,1227.604,1228.612,1228.739,1229.383,1231.391,1248.426,1251.164, 1260.422 , 1264.738 , 1265.002 , 1304.370 , 1305.592 , 1309.276 ,1350.072
Si III	1206.500, 1294.545 , 1296.726 , 1298.946 , 1301.149 , 1303.323
Si IV	1393.755,1402.770
P II	1152.818, 1153.995 ,1155.014,1156.970,1159.086,1231.184,1249.830,1310.703
P III	1334.813, 1344.326
S I	1191.895,1197.548,1425.030
S II	1166.291,1167.512,1233.438, <i>1250.584</i> , 1253.811 , 1259.519
S III	1194.041,1200.956
Ca II	3934.778 ,3969.592,8544.435
Cr II	1247.555,1248.219,1398.430,1426.206,1430.853,1431.320,1431.868,1432.056,1432.375,1433.007
Cr III	1136.657,1144.089,1146.329,1154.099, 1161.421 ,1197.341,1201.401,1204.913,1206.370,1209.119,1211.108,1221.059,1221.887,1225.632,1228.643,1231.857,1232.960,1236.180,1238.511,1247.831, 1252.601 , 1259.004 ,1261.849,1263.596,1264.197,1269.092
Fe II	1130.443,1133.405,1133.665,1133.675,1138.632, 1142.312 ,1142.336,1142.474, 1143.226 ,1144.049, 1144.274 , 1144.939 ,1146.364, 1146.833 , 1146.952 , 1147.352 ,1147.409,1148.072, 1148.081 , 1148.277 ,1148.682,1148.945,1148.956, 1149.615 ,1149.953,1150.289, 1150.468 , 1150.685 , 1151.146 ,1152.874, 1153.272 , 1154.397 ,1157.631,1159.339,1164.867, 1166.035 ,1166.974,1168.492,1169.190, 1170.292 ,1175.681,1183.829,1192.030,1198.932,1199.237,1199.672,1200.240,1219.798,1224.130,1225.496,1228.521,1230.917,1230.927,1260.536,1260.827,1262.142,1265.641,1266.254,1266.679, 1267.425 ,1271.986,1272.617,1275.782,1275.822,1277.647,1290.193,1296.696,1300.047,1309.551,1311.063, 1358.935 , 1359.055 ,1361.363, 1361.374 ,1362.754,1364.579,1366.391,1366.723, 1368.094 ,1371.028,1373.718, 1375.175 ,1377.986, 1379.469 ,1383.580, 1387.218 , 1392.148 ,1392.817,1397.578,1408.484,1412.842,1413.706,1417.738,1420.916,1424.717,1430.781,1430.888,1448.401
Fe III	1130.397,1131.189,1131.908, 1142.455 ,1142.950, 1143.666 ,1214.562
Ni II	1133.730,1134.533,1137.090,1139.638,1140.459,1154.419, 1164.279 , 1164.575 , 1168.041 , 1171.291 , 1173.477 , 1317.217 , 1335.201 , 1370.132 , 1381.286 , 1393.324 ,1411.065